Environmental Science Processes & Impacts

ROYAL SOCIETY OF CHEMISTRY

PAPER

View Article Online
View Journal | View Issue

Cite this: *Environ. Sci.: Processes Impacts*, 2025, **27**, 3641

An annular cylindrical oxidation flow reactor: hydrodynamic characterization and validation for gas-particle processing studies

Beristain-Montiel Erik, *[a] Cisneros-Vélez Mariana,[a] Villarreal-Medina Rodrigo,[a] Ramírez-Argáez Marco Aurelio,[a] Peralta Oscar,[b] Castro Telma,[b] Salcedo Dara[c] and Torres-Jardón Ricardo[b]

Oxidation flow reactors (OFRs) are essential tools for simulating atmospheric aging of aerosols, yet conventional laminar-flow designs often suffer from non-uniform oxidant exposure, broad residence time distributions (RTDs), and significant wall losses, limiting their ability to replicate real-world gas-and-particle-phase processes. Here, we present the design, hydrodynamic characterization, and experimental validation of a novel Annular Cylindrical Oxidation Flow Reactor (AC-OFR) featuring an optimized annular-flow geometry. Using computational fluid dynamics (CFD) simulations and a full factorial design of experiments, we identified reactor dimensions that minimize recirculation and dead volume, achieving RTDs approaching ideal plug flow for both gases and particles. Experimental measurements confirmed high transmission efficiencies for ozone, sulfur dioxide, and particles (50–800 nm), with strong gas-particle coupling and minimal wall losses. The AC-OFR enables precise, tunable oxidant exposures—reaching OH radical exposures equivalent to 0.5–15.3 days with 7 s^{-1} of external OH reactivity added and ozone exposures up to 0.74 days of atmospheric aging—by adjusting the UV lamp free surface. Validation experiments with α-pinene demonstrated steady-state secondary organic aerosol (SOA) yields (0.11–0.14) consistent with or exceeding those reported for traditional OFRs and revealed robust nucleation and growth dynamics. The AC-OFR thus provides a flexible, high-performance platform for controlled gas and gas-particle oxidation studies, bridging laboratory experimentation and atmospheric processes.

Received 29th May 2025
Accepted 6th October 2025

DOI: 10.1039/d5em00412h

rsc.li/espi

Environmental significance

The annular oxidation flow reactor (AC-OFR) developed in this study enables precise simulation of atmospheric oxidation processes, providing new insight into the formation and aging of secondary organic aerosols under environmentally relevant conditions. By combining improved flow dynamics, high transmission efficiency, and tunable oxidant exposures, the AC-OFR overcomes key limitations using accessible, reliable instrumentation and allows for accelerated, yet realistic, laboratory studies of multiphase atmospheric chemistry comparable to other OFRs. This advancement directly supports improved understanding of aerosol impacts on air quality and climate and provides a robust platform for evaluating the environmental fate and transformation of organic compounds, thereby informing both regulatory science and atmospheric process modeling.

Introduction

Atmospheric aerosols play critical roles in climate regulation, air quality, and human health by influencing radiative forcing, cloud formation, and heterogeneous chemical processes. Understanding the aging and transformation of aerosols in the atmosphere is essential for accurately predicting their impacts.[1] Laboratory tools such as oxidation flow reactors (OFRs) have become indispensable for simulating these processes under controlled conditions by exposing aerosols to elevated concentrations of oxidants like OH, O_3, and NO_3 radicals.[2] However, despite their widespread use, conventional OFR designs face significant limitations in replicating real-world atmospheric conditions, particularly when studying complex systems involving gas-particle interactions.[3]

Traditional OFRs, such as the Potential Aerosol Mass (PAM) reactor, often employ laminar flow regimes where radial concentration gradients and axial dispersion can lead to non-uniform oxidation conditions.[4,5] This lack of homogeneity

[a]*Facultad de Química, Universidad Nacional Autónoma de México, 3000 Universidad Av., Coyoacán, CDMX, Mexico, 04510. E-mail: erickbm@comunidad.unam.mx*
[b]*Instituto de Ciencias de la Atmósfera y Cambio Climático, Universidad Nacional Autónoma de México, 3000 Universidad Av., Coyoacán, CDMX, Mexico, 04510*
[c]*Unidad Interdisciplinaria de Docencia e Investigación Juriquilla, Facultad de Ciencias, Universidad Nacional Autónoma de México, Blvd, Universitario 3001, Querétaro, Mexico, 76230*

introduces uncertainties in the residence time distributions (RTDs) and oxidant exposure, which are critical for accurately simulating aerosol aging. For example, Xu *et al.* (2024)[6] reported that laminar-flow OFRs exhibit long RTD tails that deviate from the ideal plug flow behaviour, complicating the kinetic interpretation of secondary organic aerosol (SOA) formation. Furthermore, the wall losses of reactive gases and particles exacerbate these challenges by distorting the measurements of oxidant exposure and particle transformation.[6]

Comprehensive reviews highlight the central role of oxidation flow reactors (OFRs) in advancing laboratory studies of secondary organic aerosol (SOA) formation and aging. Ma *et al.* (2025)[7] detail how OFRs have evolved from early laminar and static reactors to more advanced designs capable of producing tuneable oxidant fields, improved mixing, and realistic atmospheric processing of volatile organic compounds (VOCs).

Recent advances have sought to address these issues through improved reactor designs that enhance mixing and minimize wall interactions.[8–10] For instance, the Accelerated Production and Processing of Aerosols (APPA) reactor introduced by Xu *et al.* in 2024[6] demonstrated narrower RTDs for both gases and particles compared to conventional OFRs, enabling more accurate simulations of aqueous-phase reactions in cloud droplets and aerosol liquid water. However, despite these innovations, most OFRs still rely on laminar flow configurations, which are inherently limited in their ability to replicate the turbulent mixing conditions found in the atmosphere.

Annular-flow geometries offer a promising alternative to conventional laminar-flow designs by promoting enhanced radial mixing and reducing the RTD variability. In annular reactors, fluid motion between concentric cylinders creates turbulent-like conditions that improve mass transfer efficiency and reduce concentration gradients.[8–10] While annular flow has been extensively studied in industrial applications such as chemical reactors,[8] its potential for aerosol research remains unexplored.

Recent advancements in oxidation flow reactors (OFRs) include the Toronto Photo-Oxidation Tube (TPOT)[5] and the Aerosol Reactor Flow tube Setup (ARFS),[11] both of which employ central UV lamps within annular or coaxial geometries to drive photochemical reactions. The TPOT consists of a glass mixing chamber and a reaction chamber configured with a central mercury pen-ray lamp emitting primarily at 254 nm, with flows designed to enable plug-flow or near-plug-flow conditions. Both TPOT and the flow tube were developed to facilitate studies of heterogeneous oxidation, transmission efficiencies, and residence time distributions (RTD) for gases and particles; they demonstrated improved RTD shape and phase coupling compared to older laminar reactors, though often with relatively high surface-area-to-volume ratios and notable wall losses for some gases (CO_2) and particles (bis(2-ethylhexyl) sebacate, BES).

The FoxBox reactor recently developed by Choudhary *et al.* in 2024[3] represents another attempt to integrate annular flow into an OFR to simulate diesel exhaust ageing. Their study demonstrated nearly 100% particle transmission efficiency across a wide size range (15–615 nm) under turbulent flow conditions, highlighting the potential of annular geometries for minimizing particle losses.

Despite these advancements, there is still a lack of comprehensive studies characterizing annular-flow OFRs for systems involving both gases and particles. Specifically, there is a need for a detailed validation of RTDs across different species (*e.g.*, reactive gases like SO_2 and particles of varying sizes) to ensure that annular-flow OFRs can accurately replicate atmospheric processes.

Accurate simulation of atmospheric aging processes requires simultaneous validation of RTDs for both gaseous and particulate species due to their distinct transport dynamics. For example, wall losses disproportionately affect smaller particles due to diffusion-driven deposition, whereas reactive gases like SO_2 may adhere to surfaces or undergo secondary reactions during transport.[12–14] Xu *et al.* in 2024[6] emphasized the importance of multi-species RTD validation in their characterization of the APPA reactor but noted that most studies focused on either gas-phase or particle-phase processes in isolation. A comprehensive approach that integrates both phases is essential for understanding coupled gas-particle interactions under realistic atmospheric conditions.

Cetyl trimethyl ammonium chloride (CTAC) serves as an ideal model system for validating OFR performance due to its well-characterized physicochemical properties. As a surfactant commonly used in aqueous aerosol studies, CTAC exhibits hygroscopic behavior with $\kappa \approx 0.12$ and forms stable particles under humidified conditions (60% RH).[15] On the other hand, α-pinene has been a reference for oxidation testing in new OFRs, and its products are representative of secondary organic aerosols formed through ozone and OH radical oxidation.[16] By monitoring changes in α-pinene composition using advanced instruments like the Aerosol Chemical Speciation Monitor (ACSM), it can directly assess the oxidative capacity and efficiency of an OFR.

This study presents the design and characterization of a novel annular-flow OFR optimized for aerosol processing under controlled conditions. The reactor features a conical diffusor leading to a cylindrical chamber with integrated UV lamps capable of generating tunable oxidant fields. Through computational fluid dynamics (CFD) simulations validated with experimental measurements, we characterize RTDs for gases (O_3, SO_2) and particles across multiple flow rates. Key contributions include: (1) hydrodynamic characterization: quantification of size-dependent particle transmission efficiencies and wall loss rates under annular flow conditions. (2) Oxidant control: demonstration of tunable OH exposure using UV lamp attenuation strategies validated through SO_2 decay kinetics. (3) Aerosol processing validation: monitoring compositional changes for α-pinene *via* ACSM to evaluate oxidative processing efficiency.

Experimental

Annular cylindrical OFR geometry design

The annular cylindrical oxidation flow reactor (AC-OFR) was designed as a PTFE cylindrical reactor with a centrally

positioned UV lamp enclosed in an ultrapure quartz tube (45.6 cm length × 2.5 cm diameter), creating an annular flow region. A full factorial experimental design (DoE 2^3) evaluated three geometric parameters: reactor radius (r_{cyl}): 28.5 mm (low) *vs.* 47.5 mm (high), Inlet diffuser angle (α): 20° (low) *vs.* 35° (high), and cylinder length (L_{cyl}): 472 mm (low) *vs.* 692 mm (high). Eight configurations were simulated (Fig. S1, Tables S1 and S2, SI) to optimize plug flow percentage while minimizing dead volume. The inlet/outlet diameters were fixed at 4 mm (stainless steel tubing compatibility).

Computational fluid dynamics (CFD) setup

Governing equations and turbulence modelling. Simulations used the k-ω SST turbulence model with low-Reynolds-number correction to capture transitional flow regimes (Re ≈ 500–3000). The steady-state Navier–Stokes equations were solved for incompressible air (ρ = 1.225 kg m^{-3}, μ = 1.789 × 10^{-5} Pa s) under isothermal conditions and the following assumptions:[17] no-slip boundary at PTFE walls, symmetry along two orthogonal planes (1/8th domain modeled), zero gauge pressure at outlet and inlet velocities of 0.21 m s^{-1} (3.5 L min^{-1}). Details of the simulations, mathematical models and assumptions are described in the SI.

Mesh generation and validation. A structured hexahedral mesh (~500k elements) was generated with local refinement near inlet/outlet regions (Fig. S2). Mesh independence was confirmed when velocity variations fell below 2% between successive refinements. The model was numerically validated against the Caltech Photooxidation Flow Tube (CPOT) reactor data,[18] achieving <5% deviation in residence time distribution (RTD) predictions (Fig. S3). Details of the eight different geometries tested through the RTDs, average residence times and percentages of piston, mixed and dead flows are described in Fig. S4 and Table S3 in the SI.

AC-OFR construction. The optimum reactor geometry was fabricated from PTFE based on the results of the experimental design of eight different geometries (details in Fig. S5, SI). The AC-OFR was constructed using polytetrafluoroethylene (PTFE) due to its exceptional chemical inertness, thermal stability, and minimal interaction with both reactive gases and particles,[19] properties that are especially advantageous in atmospheric simulation and oxidation flow reactor studies.[6,14]

The main chamber was 69.2 cm in length × 9.5 cm in diameter, while the synthetic quartz UV-lamp enclosure (Helios quartz America, USA, >80% UV transmittance between 170 and 300 nm), with the dimensions of 45.6 cm × 2.5 cm (housing an 18 W Hg lamp, λ = 185 nm), was located in the center of the main chamber and coming in from the exit of the AC-OFR. Temperature control in the AC-OFR was done by passing a stream of nitrogen at 2.0 L min^{-1} inside the UV lamp enclosure at all times during an experiment.

At 23 cm from the reactor's ending, a circular port 25 mm in diameter was used to measure UV irradiance (UVC meter, Extech SDL470, USA). Meanwhile, temperature and relative humidity (BME480 sensor, Bosch) were measured in a PTFE chamber next to the UV meter port. The inlet diffuser was

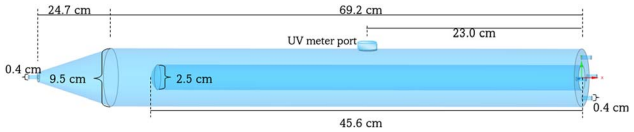

Fig. 1 Geometry and dimensions in centimeters of the AC-OFR, completely made with PTFE except the inner cylinder (UV lamp enclosure) made of high purity quartz.

24.7 cm in height, with a 20° expansion angle. The outlet configuration of the AC-OFR consists of four radially distributed ports (6.35 mm diameter each) positioned around the central quartz tube. These outlets are combined into a single common sampling line, from which multiple gas- and particle-phase instruments are connected *via* T-shaped derivations. This unified sampling approach ensures that both gases and aerosols experience the same residence time distribution (RTD) post-reactor and minimizes differences in transport and wall losses between sampling lines.

The total reactor volume was 4.05 L with a surface-to-volume ratio of 56.4 m^{-1}considering the inner quartz tube for the UV lamp enclosure and the inner PTFE walls of the reactor (*vs.* 23–74 m^{-1} in conventional OFRs). Fig. 1 shows the geometry and dimensions of the AC-OFR.

Tracer experiments. For gases one second pulse of ozone (O_3, 15 ppm) was generated *via* corona discharge (Pinus Longaeva, China) or sulfur dioxide (SO_2, 1 ppm in N_2 balance, Infra, Mexico) was sent through the AC-OFR at 3.5 L min^{-1} using zero air as carrier gas. An ozone analyzer (49i, Thermoscientific, USA) and a SO_2 monitor (100A, API, USA) were used to measure gas concentrations at the exit of the reactor. In the case of particles, monodisperse CTAC aerosols (100–800 nm, 50 nm steps) were generated *via* an atomizer coupled to an electrostatic classifier (TSI 3086/3080, USA). The CTAC particles were employed due to their well-defined physicochemical properties and excellent stability under humidified conditions. The hygroscopic nature of CTAC allows for consistent and reproducible particle generation across the tested size range, making it particularly suitable for evaluating particle-phase transmission efficiency and wall losses within the reactor.[20]

The total flow rates were 2.0, 3.5, and 5.0 L min^{-1} (ultra-dry zero air carrier, Infra, Mexico). The particle concentration was measured by a Condensation Particle Counter (CPC 3787, TSI, USA) at the exit of the AC-OFR. In all cases, the AC-OFR was deep cleaned between experiments and passivated with 10-minute preconditioning with tracer-free flow.

The average residence time distribution (τ) was calculated from the residence time distribution function (RTD) according to eqn (1), where $C(t)$ is the tracer concentration at time t. Meanwhile, the transmission efficiency (η) was determined using eqn (2) by comparing 10-minute constant flow of tracers passed through the AC-OFR in comparison to a bypass line (stainless steel tube, 4 mm internal diameter).

$$\tau = \frac{\int_0^\infty tC(t)\mathrm{d}t}{\int_0^\infty C(t)\mathrm{d}t} = \int_0^\infty t\cdot \mathrm{RTD}\cdot \mathrm{d}t \quad (1)$$

$$\eta = \frac{C(t)_{\text{AC-OFR}}}{C(t)_{\text{Bypass line}}} \quad (2)$$

Oxidant concentration. The AC-OFR was connected at the exit to a Condensation Particle Counter (CPC, 3086 TSI, Inc., USA), a Differential Mobility Analyzer (DMA, 3080, TSI, Inc. USA), an ozone and a sulfur dioxide monitor and an Aerosol Chemical Speciation Monitor (ACSM, Aerodyne Inc. USA), for particle size distribution, gas concentration and aerosol composition analysis. At the AC-OFR inlet, gases were introduced at a constant total flow rate of 3.5 L min^{-1}, precisely controlled using electronic mass flow controllers (MF5700, Siargo, China) and manually fine-tuned with needle valves (Swagelok, Germany). To maintain controlled humidity conditions, the carrier gas was humidified by passing zero air through a bubbler (for RH < 59%) or an atomizer (model 3076, TSI Inc., USA, for RH > 59%) filled with deionized distilled water, followed by filtration to remove large droplets. Temperature, pressure, and relative humidity were continuously monitored immediately upstream of the reactor inlet using a BME480 sensor (Bosch, Germany). A schematic of the AC-OFR and the instrument configuration is presented in Fig. 2, with arrows indicating the direction of flow.

The concentrations of key oxidants such as ozone (O_3) and hydroxyl radicals (OH) within the AC-OFR were quantified by operating the reactor in OFR185 mode, which utilizes a 185 nm UV lamp to generate oxidants *in situ*. The OH exposure was precisely controlled by exchanging UV lamps with varying free surface, due to lamp covering by shielding in segments the UV lamp surface with black thermofit tape (polyolefin heat-shrink tubing), ranging from 50% to 99% of the total UV lamp surface, thereby regulating the intensity of UV irradiation and the resulting oxidant production. Attenuation of the UV lamp with shielding >90% was applied by adjusting the voltage (1–10 volts) of a dimming ballast (Lutron Eco 10, USA) to reach the lowest OH exposures (<7 days). UV irradiance uniformity was tested by placing the UV probe at different positions around the UV-lamp inside the reactor, and no differences in measurements were found. Ozone was generated through the photolysis of molecular oxygen (O_2) in dry air, while OH radicals were produced *via* the photolysis of water vapor (H_2O).

Three experimental modes were fundamental for determining oxidant concentrations and for conducting SOA precursor oxidation experiments in the AC-OFR: photolysis, O_3exp, and OHexp modes. In Photolysis mode, only nitrogen was used as the carrier gas with the UV lamp activated; under these conditions, no oxidants are formed, and chemical processes are driven solely by 185 nm and 254 nm UV radiation. This mode is also essential for reactor cleaning, as it facilitates the removal of residual reactants and products between experiments. In O_3exp mode, dry air serves as the carrier gas, and ozone is generated *via* O_2 photolysis when the UV lamp is on, enabling the study of ozone-specific reactions. Finally, OHexp mode employs humidified zero air (59% relative humidity) as the carrier gas, allowing for the *in situ* generation of OH radicals upon UV irradiation; this mode is used to investigate SOA formation from OH-initiated oxidation of precursors.

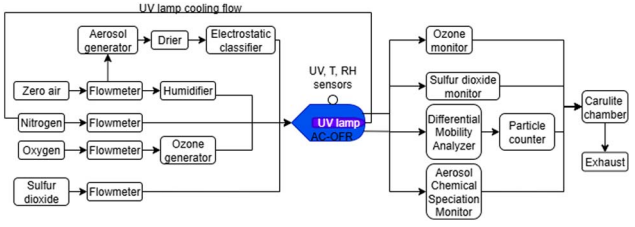

Fig. 2 Peripheral and measurement instrument configuration around the AC-OFR.

Hydroxyl radical concentrations were quantified using SO_2 as a chemical tracer. A gas mixture consisting of zero air (2.5 L min^{-1}) and sulfur dioxide (SO_2, 1.0 L min^{-1} at 1 ppm in nitrogen balance) was continuously passed through the reactor. After a 10-minute stabilization period to ensure steady-state conditions, the initial SO_2 concentration was recorded using a gas monitor. Upon activation of the 185 nm UV lamp, OH radicals generated inside the reactor reacted with SO_2, causing a measurable decrease in SO_2 concentration. The hydroxyl radical exposure, $[OH]_{exp}$, was calculated assuming a pseudo-first-order reaction using the rate constant for the OH + SO_2 reaction, $k_{OH+SO_2} = 9.49 \times 10^{-13}$ cm^3 $molecule^{-1}$ s^{-1}, applying eqn (3).[21,22]

$$OH_{exp} = \frac{1}{k_{OH+SO_2}} \ln \frac{[SO_2]_0}{[SO_2]_t} \quad (3)$$

For those cases where VOCs were added (*i.e.*, α-pinene), OH exposure was corrected by OH reactivity according to Peng *et al.* (2015).[2,23]

Organics oxidation experiments. To evaluate the oxidative capacity and applicability of the AC-OFR for atmospheric chemistry studies, a series of organic oxidation experiments were performed under controlled humidity and flow conditions. The focus was on the formation of secondary organic aerosol (SOA) and the quantification of SOA yields.

For gas-phase experiments, α-pinene vapor was introduced by passing zero air through a sealed flask containing the liquid precursor and then mixed with humidified air (59% RH). In both cases, the total flow through the AC-OFR was maintained at 3.5 L min^{-1}, and the relative humidity was controlled at 59% using a water bubbling humidification system.

Prior to initiating oxidation, a 15-minute stabilization period was allowed to ensure steady-state concentrations of gas-phase precursors within the reactor. Aerosol concentrations were measured using a Scanning Mobility Particle Sizer (SMPS, *i.e.* CPC 3086 and DMA 3081) and an Aerosol Chemical Speciation Monitor (ACSM, Aerodyne). The α-pinene precursor concentration was calculated by gravimetric analysis of the vial containing the compound (details in the SI).

Photochemical oxidation was initiated by activating the centrally positioned UV lamp (185 nm) inside the AC-OFR. The SOA yield was calculated as the ratio of the net increase in aerosol mass concentration (as measured by the ACSM or SMPS)

to the mass of precursor consumed during the oxidation process (eqn (4)).

$$Y = \frac{\Delta M_{\mathrm{SOA}}}{\Delta M_{\mathrm{precursor}}} \quad (4)$$

where ΔM_{SOA} is the difference in aerosol mass concentration before and after UV exposure, and $\Delta M_{\mathrm{precursor}}$ is the mass of precursor consumed, determined gravimetrically (for α-pinene). When the ACSM was not available, the total particle mass calculated through eqn (5) was employed as ΔM_{SOA}. Nucleation rates were calculated as the maximum rate of increase in particle number concentration ($\mathrm{d}N/\mathrm{d}t$) within 1.7 to 10 nm diameter during the oxidation stages.

$$\Delta M_{\mathrm{SOA,\ SMPS}} = \sum_i N(D_{\mathrm{Pi}}) \cdot \frac{\pi}{6} {D_{\mathrm{Pi}}}^3 \rho \Delta \log D_{\mathrm{P}} \quad (5)$$

where $N(D_{\mathrm{Pi}})$ is the number concentration per bin, (D_{Pi}) is the diameter mid-point, ρ is the particle density (1.2 g cm^{-3} for a typical SOA), and $\log D_{\mathrm{P}}$ is the width of the log-diameter bin. $\Delta M_{\mathrm{SOA,SMPS}}$ was also used to validate ACSM measurements when available, and a 20–30% difference between SMPS and ACSM measurements was considered as adequate according to Watson *et al.* (2020).[24]

All yields were corrected for wall losses *via* instrument transmission efficiency, as described in Section 2.4. Each experiment was performed in triplicate to ensure reproducibility. The reported SOA yields represent the mean values, with uncertainties given as the standard deviation of the replicates.

Results and discussion

Optimum AC-OFR geometry

The Annular Cylindrical Oxidation Flow Reactor (AC-OFR) introduces a novel annular flow geometry, distinct from conventional tubular OFR designs. Annular flow configurations inherently reduce radial concentration gradients, enhance species mixing, and minimize recirculation zones, critical advantages for achieving uniform oxidation conditions. To identify the optimal AC-OFR geometry, a 2^3 full factorial experimental design (DoE) was implemented,[25] evaluating three factors: reactor radius, diffuser angle, and cylinder length.

While initial simulations suggested minimal differences in piston flow percentage ($p > 0.05$) across the eight configurations, the deviation between CFD-predicted residence times (τ_{CFD}) and theoretical residence times ($\tau_{\mathrm{th}} = V/Q$) emerged as a critical metric for reactor optimization (Fig. S4 and Table S3). This discrepancy, termed $\Delta\tau = |\tau_{\mathrm{CFD}} - \tau_{\mathrm{th}}|$, served as the desirability function in the DoE. Smaller $\Delta\tau$ values indicate closer alignment with ideal plug flow behaviour, a key criterion for OFR performance. The DoE framework prioritized configurations where $\Delta\tau \leq 10\%$ of τ_{th}, leveraging prior validation of the CFD model against the Caltech Photooxidation Flow Tube.[18]

The CFD simulations revealed a $\Delta\tau$ (discrepancy between modelled and theoretical residence times) ranging from 0.2 to 9.2 seconds, with smaller-volume reactor configurations exhibiting higher deviations. While the constructed AC-OFR ranked third lowest in $\Delta\tau$ (1.7 s at 3.5 L min^{-1}), its selection

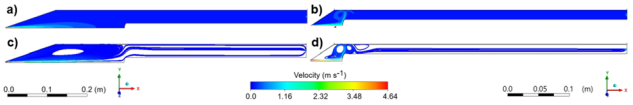

Fig. 3 CFD analysis of the AC-OFRs: (a) velocity profiles for the constructed AC-OFR (high-volume, reactor B, Table S2) and (b) one of the small-volume OFR designs (reactor G, Table S2), (c) flow streamlines for the constructed high-volume AC-OFR and (d) one of the small-volume OFR designs.

was driven by superior hydrodynamic performance and practical scalability. Larger-volume designs demonstrated reduced axial dispersion and a lower surface-to-volume ratio (56.4 m^{-1} *vs.* 128.1 m^{-1} for smaller reactors, Table S2), minimizing wall interactions and recirculation zones. These characteristics align with the need for uniform oxidation conditions in atmospheric simulations, where radial mixing and minimized stagnation are critical. Experimental validation further confirmed the selected AC-OFR enhanced plug flow behaviour.

In comparison, the Annular Cylindrical Oxidation Flow Reactor (AC-OFR) represents a significant advancement over previous annular designs such as the Toronto Photo-Oxidation Tube (TPOT)[5] and the Aerosol Reactor Flow Setup (ARFS).[11] It integrates a fully optimized annular geometry, designed and refined through computational fluid dynamics (CFD) simulations, with chemically inert PTFE construction and a modular central 185 nm UV lamp. A key innovation is the inclusion of a carefully engineered inlet diffuser, which effectively reduces flow stagnation and establishes a near-laminar flow profile prior to the oxidation zone, thereby enhancing uniform exposure to UV irradiation around the lamp and improving reaction homogeneity as discussed from Fig. 3.

Fig. 3 shows the velocity profiles and flow streamlines between the AC-OFR chosen for construction and one of the small volume reactors. Both exhibited recirculation in the diffusor inlet region. However, recirculation impacted the smaller OFR higher due to the closeness of the UV-lamp enclosure to the inlet. This OFR displayed recirculation and mixing in the region around the UV-lamp, which can negatively impact the reactivity of species (*i.e.* 2nd generation or more reactions, non-atmospheric relevant reactivity or particle formation). Meanwhile, the selected OFR showed recirculation close to the inlet but with a lower impact around the UV-lamp enclosure. The higher diameter, the less pronounced the diffusor angle and the longest distance between the inlet and the UV lamp produced a higher degree of plug and laminar flow around the UV lamp. This analysis is in agreement with the conclusions made in other reported reactors. For example, Xu & Collins (2021) and Huang *et al.* (2017)[14,18] recommended diffusor inlet angles lower than 35° and 37°, respectively to prevent recirculation and dead flow regions. These results not only demonstrate near plug flow conditions around the reaction zone within the AC-OFR but also indicate that oxidant exposure in the reaction chamber is largely uniform and minimally influenced by flow dynamics in the inlet region.

Residence time distribution (RTD)

The probability distribution function (PDF) of the residence time describes how long particles or gases stay inside a reactor before exiting. This function is normalized so the total probability integrates to one. The PDF is a useful tool that aids comparing different reactors independently of their geometry and dimensions.[17] Fig. 4 shows the comparison of the PDFs of different reported reactors in the literature[5,6,14,26] including the AC-OFR.

The residence time distribution (RTD) characteristics of the AC-OFR (Fig. 4, orange lines) reveal important flow dynamics that position this reactor design between ideal plug flow and complete mixing regimes.[27] For gas-phase transport (Panel a), the AC-OFR exhibits a moderately sharp peak at approximately 0.6–0.7 normalized residence time, followed by an extended tail-a profile intermediate between PAM-OFR's[5] broad distribution and APPA's[6] pronounced plug-flow behaviour. This indicates efficient radial mixing despite the annular configuration, likely attributable to the reactor's optimized geometry. Notably, the particle-phase RTD (Panel b) closely mirrors the gas-phase behaviour, with similar peak timing and tail characteristics, demonstrating exceptional gas-particle coupling, a critical advantage for oxidation studies.

The extended tail observed in the residence time distributions (RTDs) for both gaseous and particulate species indicates the presence of recirculation or stagnation zones within the AC-OFR. However, these effects are considerably less pronounced than in traditional laminar flow designs. Computational fluid dynamics (CFD) simulations (Fig. 3) reveal that recirculation primarily occurs in the inlet diffuser region upstream of the oxidation zone, promoting effective mixing before photochemical reactions occur around the UV lamp. This spatial separation ensures that the reaction chamber maintains predominantly near-laminar and plug-flow behaviour, minimizing axial dispersion and non-uniform oxidant exposure. Consequently, the AC-OFR design balances enhanced pre-reaction mixing with uniform flow during oxidation, improving reaction homogeneity and reproducibility while limiting wall losses. This distinction is critical for accurate kinetic analyses and represents a key improvement over reactors where recirculation extends into the reaction region.

These characteristics make the AC-OFR particularly suitable for oxidation studies requiring moderate-to-long residence times with uniform oxidant exposure, as the balance between

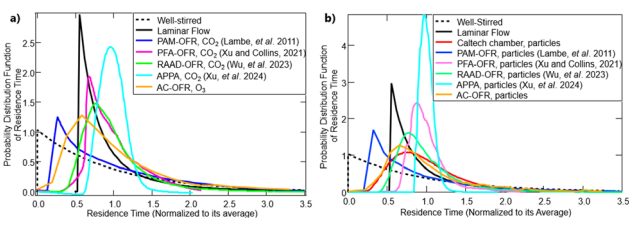

Fig. 4 Probability Distribution Function (PDF) of the residence time for the PAM-OFR (Lambe *et al.*, 2011), PFA-OFR (Xu and Collins, 2021), RAAD-OFR (Wu *et al.*, 2023), APPA (Xu *et al.*, 2024) and the AC-OFR for (a) gases and (b) particles.

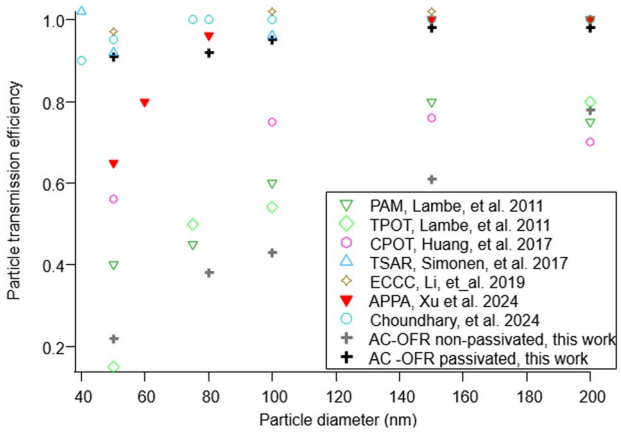

Fig. 5 Comparative particle transmission efficiency between the AC-OFR and similar OFRs reported in the literature.

mixing efficiency and reduced wall effects enables more accurate simulation of atmospheric aging processes.

Transmission efficiencies through the AC-OFR were high, averaging 0.98 ± 0.11 for O_3, 0.95 ± 0.12 for SO_2, and 0.91 ± 0.14 for CTAC particles, with particle transmission found to be independent of size (ANOVA, $p > 0.05$) in the range between 50 and 800 nm. These efficiencies were achieved only after a mandatory 10-minute passivation period with tracers, which is critical to saturate reactive sites on reactor surfaces; insufficient passivation led to drastic efficiency drops below 0.4. Compared to other reactors, these results align well with those of Lambe *et al.* (2011),[5] who reported transmission efficiencies of 0.97 ± 0.10 for CO_2 and 1.2 ± 0.4 for SO_2 in the larger (15 L) Potential Aerosol Mass (PAM) chamber, and with those of Xu and Collins (2021),[14] who observed somewhat lower efficiencies (0.90 ± 0.02 for CO_2 and 0.76 ± 0.04 for SO_2) in an all-Teflon reactor of different geometry. Xu's work further highlighted that removing internal and external electrostatic charges enhances transmission efficiency, underscoring the importance of surface conditioning. Fig. 5 resumes the comparison of particle transmission efficiency across different designs of OFRs.

Table 1 shows the comparison of average residence times for O_3, SO_2, and particles in the AC-OFR across different flow rates and highlights the reactor's effective mixing and phase coupling, as well as the influence of species-specific interactions. At 3.5 L min^{-1}, both O_3 and particles exhibit similar average residence times (76 ± 8 s and 75 ± 4 s, respectively),

Table 1 Average residence times of ozone, sulphur dioxide and CTAC particles in the AC-OFR

Species	τ (s) at 2.0 L min^{-1}	τ (s) at 3.5 L min^{-1}	τ (s) at 5.0 L min^{-1}
O_3	80 ± 9	76 ± 8	68 ± 4
SO_2	158 ± 12	92 ± 4	71 ± 1
Particles	122 ± 5	75 ± 4	65 ± 3
Volume/flow rate	121.5	69.4	48.6

closely matching the theoretical value calculated from the reactor volume and flow (69.4 s). This close agreement indicates efficient gas-particle coupling and suggests that the annular flow configuration of the AC-OFR minimizes differential transport between phases, a common limitation in other OFR designs.

In contrast, SO_2 consistently displays longer residence times, particularly at lower flow rates (*e.g.*, 158 ± 12 s at 2.0 L min^{-1}), which is indicative of stronger wall interactions or surface adsorption effects unique to this tracer. As the flow rate increases, the residence times of all species converge toward the theoretical value, reflecting enhanced turbulent mixing and reduced wall effects at higher Reynolds numbers. These results demonstrate that the AC-OFR provides a favourable balance between sufficient residence time for oxidation processes and minimized wall losses, with 3.5 L min^{-1} representing an optimal operational point for atmospheric simulation experiments.

OH and O_3 exposure

Oxidant concentrations in the AC-OFR were systematically quantified through dedicated experimental modes. Ozone concentration was determined in O_3exp mode using dry air as carrier gas, while hydroxyl radical concentration was measured in OHexp mode using humidified air (59% RH) with sulfur dioxide as a chemical tracer. Temperature was kept between 22 and 24 °C measured at the inner wall of the AC-OFR, next to the UV sensor, besides, the UV lamp was cooled by a nitrogen flow inside the quartz enclosure. Fig. S6 in the SI displays temperature and relative humidity variations during an experiment with the UV lamp on and off at different time segments.

In the AC-OFR, observed temperature increases were modest under typical operating conditions, with stable readings on the inner wall even during extended irradiance periods (Fig. S6). These results suggest effective thermal dissipation in the AC-OFR geometry, minimizing temperature hotspots that could bias reactive uptake or partitioning processes. Nevertheless, it is important to note that, due to the thermometer's location, local temperature maxima near the lamp may not be fully captured; as Pan *et al.* (2024)[28] show, such microenvironments can drive enhanced evaporation or reaction rates. While the measured wall temperatures in the AC-OFR were within 1–2 °C of ambient temperature, a more detailed temperature profiling—similar to the multi-point approach by Pan *et al.*—would allow for a finer assessment of heat effects and their chemical implications.

To establish a precise relationship between operational parameters and oxidant generation, nine distinct exposure levels were achieved by varying the central UV lamp's surface coverage (50, 60, 70, 80, 90, 91, 93, 97 and 99%). Fig. 6 shows the dependence of OH exposure dependence with the UV irradiance while Fig. S7 in the SI exhibits the O_3 concentration related to UV irradiance measurements. Fig. 6 also displays the corresponding OH exposure due to addition of α-pinene at 7 s^{-1} OH reactivity ($k_{OH,pinene}$ = 5.1 × 10^{11} cm^3 $molec^{-1}$ s^{-1}), and an extreme and non-atmospheric relevant case at α-pinene OH reactivity of 143 s^{-1}.

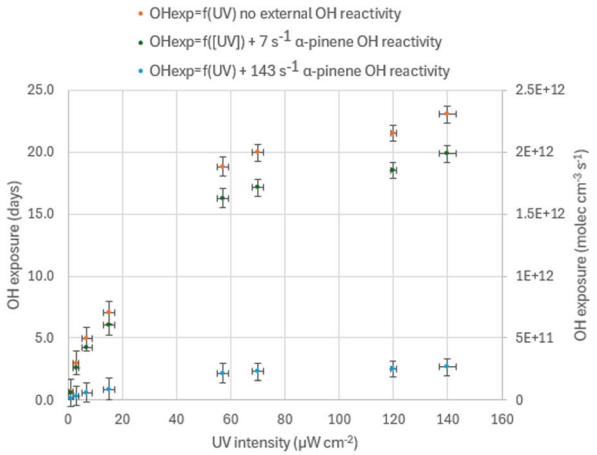

Fig. 6 Experimental OH exposures in the AC-OFR as a function of the UV intensity.

The results shown in Fig. 6 illustrate the critical role of external OH reactivity in determining the effective OH exposure within the AC-OFR. In the absence of external OH reactivity (*i.e.*, only SO_2 present at 600 ppb), the measured OH exposure reaches its theoretical maximum, corresponding to scenarios with the highest degree of oxidation, consistent with prior OFR studies such as that of Lambe *et al.* (2011),[5] who reported optimal measured exposures approaching ~2.5 × 10^{12} molec cm^{-3} s at high UV settings. Introducing moderate external OH reactivity (7 s^{-1}, typical of α-pinene experiments) reduces the measurable OH exposure by approximately one third, matching the predicted correction factor (0.67) from Peng *et al.* (2015),[2,23] and paralleling the 25–50% reductions observed in atmospheric simulation studies where VOC loads are high.

Under extremely high, non-atmospheric OH reactivity conditions (143 s^{-1}), the measured OH exposure collapses to only about 9% of the reference, directly reflecting the overwhelming competition from non-tracer VOCs, in agreement with both Peng *et al.*'s (2015)[2] modelling results and high reactivity experiments reported by Palm *et al.* (2016),[29] which emphasize that exposures above ~20 s^{-1} are rarely environmentally relevant due to such drastic diminishment in oxidant dose.

Relative humidity (RH) is another important factor that can significantly affect OH exposure measurements by influencing the solubility and uptake of SO_2 during the determination process. Our measurements at RH levels of 68% and 76% showed reductions in SO_2 transmission of 12% and 28%, respectively, compared to the 59% RH condition, which had a transmission efficiency of 0.95 ± 0.12. While Peng *et al.* (2015, 2020)[2,23] recommend using high relative humidity as safe operating conditions, our results indicate that at elevated RH, SO_2 can be lost through condensation and chemical conversion in the wet sections of the AC-OFR, rather than accurately reflecting oxidant concentrations in the gas phase. Therefore, we do not recommend determining OH exposure using SO_2 measurements at high relative humidities above 70%. Other authors have discussed this before for secondary inorganic aerosol,[30,31] leading to the same conclusions.

An average global OH concentration of 1.5×10^6 molecules cm^{-3} (ref. 32 and 33) was used to calculate the equivalent atmospheric exposure time for OHexp, while an average tropospheric ozone concentration of 7×10^{11} molecules cm^{-3} (ref. 34 and 35) was used for O_3exp. Based on these reference values, the AC-OFR demonstrates exceptional oxidative capacity, achieving OH exposures equivalent to approximately 0.7–23 days of atmospheric aging in the absence of external OH reactivity (*i.e.* VOCs added), while simultaneously providing O_3 exposures ranging from 0.1–0.74 days. This dual-oxidant capability positions the AC-OFR favourably among contemporary flow reactors.

It is important to clarify that the OH radical exposures reported were determined in the absence of any externally added volatile organic compounds (VOCs). These baseline measurements represent the intrinsic oxidative capacity generated solely from background water vapor and oxygen photolysis within the AC-OFR. The presence of added VOC precursors introduces additional external OH reactivity that can significantly reduce the effective OH exposure available for oxidation.

Consequently, the OH exposures reported here characterize the maximum achievable radical concentrations under clean, controlled conditions and serve as a reference for subsequent experiments involving reactive organic species. Corrected OH exposures should consider OH reactivity based on added VOC concentration and VOC – OH reaction rate constant as suggested by Peng *et al.* (2015).[23,36] In this regard, when external OH reactivity (7 s^{-1}) was added (α-pinene), the equivalent OH exposure was reduced to the 0.5–15.3 days range. Under non-atmospheric relevant conditions like extremely high OH reactivity, the OH exposure was reduced in the range between 0.1 and 2.0 days.

Compared to traditional environmental chambers, which typically reach an inherent upper limit of only 1–2 days of equivalent atmospheric aging, the AC-OFR provides significantly extended oxidation timescales. Even large-volume chambers like SAPHIR (270 m^3)[37] and PHOTO-LAC (1800 m^3)[38] cannot approach the tropospheric residence times of up to two weeks that our AC-OFR readily achieves.

When compared directly to other OFRs, the AC-OFR's performance is particularly noteworthy. The PAM-OFR, a widely used benchmark system, typically operates at OH exposures of approximately 10^{12} molecules per cm^3 s (equivalent to ~10 days of atmospheric aging),[5,39] while our reactor achieves similar exposures up to $2.33–3.11 \times 10^{12}$ molecules per cm^3 s employing a single UV lamp instead or two or more. More recent designs like the RAAD-OFR[26] and APPA[6] (shown in Fig. 4) have improved flow characteristics similar to the AC-OFR but have not documented equivalent oxidation capabilities reaching 3 weeks of atmospheric aging.

SOA yield

Secondary organic aerosol (SOA) yields from α-pinene oxidation in the AC-OFR were determined at four hydroxyl radical exposure (OHexp) levels, corresponding to 4.7 ± 0.9, 3.3 ± 1.0, 2.0 ± 0.4 and 0.5 ± 0.3 days of equivalent atmospheric aging when 7 s^{-1} of OH reactivity was added. Yields were calculated using eqn (4) after allowing 15 minutes stabilization under steady-state conditions. Fig. 7 shows the time series of particle number concentrations and SOA mass concentration during α-pinene oxidation. Besides, an example of non-atmospheric relevant experiments is shown in Fig. S9 in the SI.

As can be seen in Fig. 7, the experiments started with α-pinene added (OH reactivity 7 s^{-1}) and no aerosol was present (blue zones). However, once oxidation takes place, particle number concentration rises rapidly mainly for particle bins between 1.7 and 40 nm. According to total particle mass concentration calculated using eqn (5), assuming SOA density of 1.25 g cm^{-3}, they were 4.44 μg m^{-3} (13:10–13:25 h), 4.39 μg m^{-3} (13:40–13:55 h), 3.93 μg m^{-3} (14:10–14:25 h) and 3.46 μg m^{-3} (14:40–14:55 h), corresponding to OH exposures of 4.7, 3.3, 2.0 and 0.5 days of atmospheric OH equivalent exposure. The SOA yields in the AC-OFR were between 0.11 and 0.14 which aligns with values reported for α-pinene oxidation in other oxidation flow reactors (OFRs) under similar low-NO_x conditions. For instance, Lambe *et al.* (2011)[5] documented yields of 0.17–0.40 in the Potential Aerosol Mass (PAM) reactor, while Bruns *et al.* (2015)[40] reported lower yields (0.05–0.20) in a different OFR design, attributing the reduction to enhanced fragmentation at high OH exposures. The AC-OFR's intermediate yield suggests a balance between functionalization and fragmentation pathways, likely influenced by its annular flow geometry, which promotes uniform mixing before oxidation occurs, and maximizes laminar flow in the oxidation around the UV lamp.

In all experiments, aerosol formation exhibited a consistent pattern: activation of the UV lamp triggered rapid SOA production within minutes, followed by a gradual decline to a stable plateau (steady state). This reduction likely reflects evaporation of semi-volatile oxidation products (SVOCs) under prolonged UV exposure, as equilibrium between gas-particle partitioning and oxidative aging was established. These results are in accordance with other studies[41] where particle concentration often exceeded 10^5 particles cm^{-3} in the 2–100 nm range, especially when using α-pinene as the precursor. The observed high particle counts do not necessarily translate

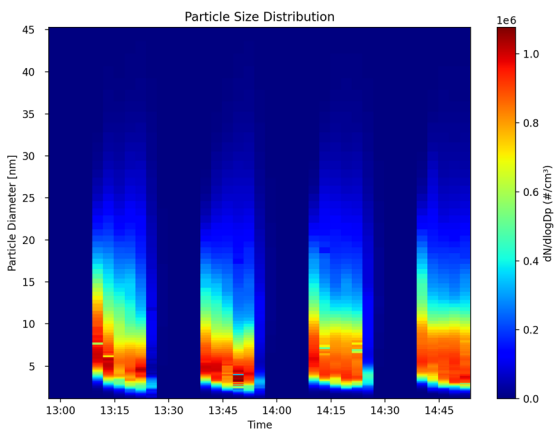

Fig. 7 Time series of particle number concentration and SOA mass concentration during α-pinene oxidation in the AC-OFR.

to large mass concentrations, because nucleation mode can dominate over the growth to larger sizes.

Fig. S9 in the SI exhibits an extreme case where a high OH reactivity (143 s^{-1}, α-pinene) was employed at high OH exposures (10^{12} molec per cm^3 per s). In this case there was a notably transient SOA peak observed in the AC-OFR that exceeded concentrations typically reported in batch-mode chambers (*e.g.*, <1000 μg m^{-3} in Nah *et al.*, 2016 (ref. 34)) but matches trends in flow reactors like the ECCC-OFR,[16] where SOA yields for α-pinene were 30–40% higher than traditional chambers due to reduced wall effects. The posterior decline in steady-state yield contrasts with studies using OFRs with shorter residence times (*e.g.*, TSAR,[13] PEAR[12]), where yields remained constant post-nucleation, suggesting the AC-OFR's extended residence time (76 ± 8 s) enhances equilibration of semi-volatile species.

The AC-OFR's performance contrasts with traditional OFRs in two key ways. First, its annular design minimizes surface interactions, reducing wall losses and enabling sustained growth of ultrafine particles (1.7–100 nm) without suppression by pre-existing aerosols-a limitation well-documented in conventional reactors.[42] Second, the AC-OFR maintains consistent nucleation rates across environmental temperature (22 °C) and humidity conditions (59% RH), unlike systems where dimer yields decline sharply under such changes,[42] likely due to optimized flow dynamics and UV homogeneity. These features underscore the reactor's ability to replicate atmospheric nucleation processes similar to laminar-flow OFRs, particularly for studies probing the interplay between highly oxygenated organic molecule (HOM)-driven nucleation and semi-volatile organic compound (SVOC) evaporation. The invariance of steady-state yields further highlights its utility for investigating SOA formation mechanisms under atmospherically relevant, controlled oxidative conditions.

Conclusions

The Annular Cylindrical Oxidation Flow Reactor (AC-OFR) developed and characterized in this study demonstrated considerable improvements over conventional OFR designs, offering enhanced hydrodynamic performance, high transmission efficiencies for both gases and particles, and precise, tunable oxidant exposures under atmospherically relevant conditions. A key innovation of the AC-OFR is the incorporation of a computational fluid dynamics (CFD)-designed inlet diffuser, which promotes effective mixing and confines turbulence and recirculation to the region before the oxidation zone surrounding the UV lamp. This design ensures a near-laminar, uniform flow around the lamp, minimizing flow stagnation and non-uniform oxidant exposure within the reaction chamber. The annular flow geometry yields residence time distributions approaching ideal plug flow, minimizes wall losses, and ensures strong gas-particle coupling, thereby reducing experimental artifacts commonly observed in laminar or tubular reactors. Transmission efficiencies averaged 0.98 ± 0.11 for ozone, 0.95 ± 0.12 for sulfur dioxide, and 0.91 ± 0.14 for particles (50–800 nm), with particle transmission independent of size. The system enables reproducible simulation of a wide range of atmospheric oxidation processes, achieving OH radical exposures equivalent to approximately 0.7–23 days of atmospheric aging in the absence of VOCs and decreasing to 0.5–15.3 days with 7 s^{-1} OH reactivity of α-pinene. Ozone exposures up to 0.74 days were also achieved. The steady-state secondary organic aerosol (SOA) yields from α-pinene oxidation were consistent with literature values (0.11–0.14) and the reactor demonstrated robust nucleation and particle growth dynamics. These features underscore the AC-OFR's suitability as a flexible, high-performance platform for controlled gas and gas-particle oxidation studies, effectively bridging laboratory experimentation and atmospheric processes.

Author contributions

Cisneros-Vélez Mariana: investigation, methodology, formal analysis, writing and editing. Villarreal-Medina Rodrigo: methodology, formal analysis, writing and editing. Ramírez-Argáez Marco Aurelio: investigation, methodology, formal analysis, writing, review, and editing. Peralta Oscar: resources, writing, review, and editing. Castro Telma: resources, writing, review, and editing. Dara Salcedo: resources, formal analysis, writing, review, and editing. Torres-Jardón Ricardo: resources, formal analysis, writing, review, and editing. Beristain-Montiel Erik: conceptualization, resources and funding acquisition, supervision, methodology, formal analysis, writing, reviewing, and editing.

Conflicts of interest

There are no conflicts to declare.

Data availability

Data for this article, including csv files for RTDs, Microsoft Excel documents with oxidant determination data, Igor Pro files for aerosol time series and txt files for particle size distribution data in the AC-OFR are available at the OSF repository at **https://osf.io/wr6vc/**. Data related to other OFRs reported in the literature should be requested to their corresponding authors.

Acknowledgements

Authors acknowledge Programa de Apoyo a Proyectos de Investigación e Innovación Tecnológica (PAPIIT IA202223) for the research grant. The authors also acknowledge the vacuum workshop at Facultad de Química, UNAM for the construction of the AC-OFR. The authors also thank Ana Karen Portillo Sánchez for the gases experiment's setup support. Rodrigo Villarreal-Medina acknowledges the Programa de Doctorado en Ingeniería Química at UNAM and CONAHCyT for the doctoral fellowship (grant number 1002868).

Notes and references

1 Z. Zhang, W. Xu, A. T. Lambe, W. Hu, T. Liu and Y. Sun, Insights Into Formation and Aging of Secondary Organic Aerosol From Oxidation Flow Reactors: A Review, *Curr.*

Pollut. Rep., 2024, **10**, 387–400, DOI: 10.1007/S40726-024-00309-7/FIGURES/2.

2 Z. Peng, D. A. Day, H. Stark, R. Li, J. Lee-Taylor, B. B. Palm, *et al.*, HOx radical chemistry in oxidation flow reactors with low-pressure mercury lamps systematically examined by modeling, *Atmos. Meas. Tech.*, 2015, **8**, 4863–4890, DOI: 10.5194/AMT-8-4863-2015.

3 V. Choudhary, Y. Xi, C. Pham, Y. Zhang, K. Hardy and C. F. Rider, Characterization and integration of a new oxidative flow reactor for use in in vitro and human exposure systems with diesel exhaust and other aerosol, *Earth, Space, and Environmental Chemistry*, 2024, DOI: 10.26434/CHEMRXIV-2024-WWT9K.

4 E. Kang, M. J. Root, D. W. Toohey and W. H. Brune, Introducing the concept of Potential Aerosol Mass (PAM), *Atmos. Chem. Phys.*, 2007, **7**, 5727–5744, DOI: 10.5194/ACP-7-5727-2007.

5 A. T. Lambe, A. T. Ahern, L. R. Williams, J. G. Slowik, J. P. S. Wong, J. P. D. Abbatt, *et al.*, Characterization of aerosol photooxidation flow reactors: Heterogeneous oxidation, secondary organic aerosol formation and cloud condensation nuclei activity measurements, *Atmos. Meas. Tech.*, 2011, **4**, 445–461, DOI: 10.5194/AMT-4-445-2011.

6 N. Xu, C. Le, D. R. Cocker, K. Chen, Y.-H. Lin and D. R. Collins, An oxidation flow reactor for simulating and accelerating secondary aerosol formation in aerosol liquid water and cloud droplets, *Atmos. Meas. Tech.*, 2024, **17**, 4227–4243, DOI: 10.5194/amt-17-4227-2024.

7 X. Ma, K. Li, S. Zhang, Z. Yang, L. Xu, N. T. Tchinda, *et al.*, Oxidation Flow Reactor and Its Application in Secondary Organic Aerosol Formation in Laboratory Studies, *ACS ES&T Air*, 2025, **2**(8), 1394–1410, DOI: 10.1021/ACSESTAIR.5C00047.

8 Y. Yan, F. Dappozze, C. Prevost, J. Ederer, J. Henych, S. Kříženecká, *et al.*, Annular flow reactor with side-by-side titania-deposited self-luminous textile and glass fiber velvet for efficient aqueous treatment of active pharmaceutical ingredients, *Chem. Eng. J.*, 2025, **506**, 159951, DOI: 10.1016/J.CEJ.2025.159951.

9 T. Tang, J. Tian, J. Deng and G. Luo, An optimized miniaturized annular rotating flow reactor for controllable continuous preparation of functionalized polysilsesquioxane microspheres, *Chem. Eng. Sci.*, 2023, **281**, 119105, DOI: 10.1016/J.CES.2023.119105.

10 M. V. Cherdantsev, S. V. Isaenkov, A. V. Cherdantsev and D. M. Markovich, Development and interaction of disturbance waves in downward annular gas-liquid flow, *Int. J. Multiphase Flow*, 2021, **138**, 103614, DOI: 10.1016/J.IJMULTIPHASEFLOW.2021.103614.

11 I. J. George, A. Vlasenko, J. G. Slowik, K. Broekhuizen and J. P. D. Abbatt, Heterogeneous oxidation of saturated organic aerosols by hydroxyl radicals: uptake kinetics, condensed-phase products, and particle size change, *Atmos. Chem. Phys.*, 2007, **7**, 4187–4201.

12 M. Ihalainen, P. Tiitta, H. Czech, P. Yli-Pirilä, A. Hartikainen, M. Kortelainen, *et al.*, A novel high-volume Photochemical Emission Aging flow tube Reactor (PEAR), *Aerosol Sci. Technol.*, 2019, **53**, 276–294, DOI: 10.1080/02786826.2018.1559918.

13 P. Simonen, E. Saukko, P. Karjalainen, H. Timonen, M. Bloss, P. Aakko-Saksa, *et al.*, A new oxidation flow reactor for measuring secondary aerosol formation of rapidly changing emission sources, *Atmos. Meas. Tech.*, 2017, **10**, 1519–1537, DOI: 10.5194/AMT-10-1519-2017.

14 N. Xu and D. R. Collins, Design and characterization of a new oxidation flow reactor for laboratory and long-term ambient studies, *Atmos. Meas. Tech.*, 2021, **14**, 2891–2906, DOI: 10.5194/AMT-14-2891-2021.

15 B. E. Swanson and A. A. Frossard, Influence of selected cationic, anionic, and nonionic surfactants on hygroscopic growth of individual aqueous coarse mode aerosol particles, *Aerosol Sci. Technol.*, 2022, **57**, 63–76, DOI: 10.1080/02786826.2022.2144114.

16 K. Li, J. Liggio, P. Lee, C. Han and Q. Liu, Secondary organic aerosol formation from α-pinene, alkanes, and oil-sands-related precursors in a new oxidation flow reactor, *Atmos. Chem. Phys.*, 2019, **19**, 9715–9731, DOI: 10.5194/ACP-19-9715-2019.

17 O. Levenspiel, *Tracer Technology Modeling the Flows of Fluids*, Springer New York, New York, NY, 1st edn, 2012, vol. 96, DOI: 10.1007/978-1-4419-8074-8.

18 Y. Huang, M. M. Coggon, R. Zhao, H. Lignell, M. U. Bauer, R. C. Flagan, *et al.*, The Caltech Photooxidation Flow Tube reactor: Design, fluid dynamics and characterization, *Atmos. Meas. Tech.*, 2017, **10**, 839–867, DOI: 10.5194/AMT-10-839-2017.

19 E. Dhanumalayan and G. M. Joshi, Performance properties and applications of polytetrafluoroethylene (PTFE)—a review, *Adv. Compos. Hybrid Mater.*, 2018, **1**, 247–268, DOI: 10.1007/s42114-018-0023-8.

20 K. A. Wokosin, E. L. Schell and J. A. Faust, Emerging investigator series: surfactants, films, and coatings on atmospheric aerosol particles: a review, *Environ. Sci.: Atmos.*, 2022, **2**, 775–828, DOI: 10.1039/D2EA00003B.

21 A. Leifer, Determination of rates of reaction in the gas-phase in the trophosphere, *Theory and Practice*, Washington, DC, 1992.

22 G. Li, H. Su, M. Li, U. Kuhn, G. Zheng, L. Han, *et al.*, Reactive uptake coefficients for multiphase reactions determined by a dynamic chamber system, *Atmos. Meas. Tech.*, 2022, **15**, 6433–6446, DOI: 10.5194/AMT-15-6433-2022.

23 Z. Peng and J. L. Jimenez, Radical chemistry in oxidation flow reactors for atmospheric chemistry research, *Chem. Soc. Rev.*, 2020, **49**, 2570–2616, DOI: 10.1039/C9CS00766K.

24 T. Watson, A. Aiken, Q. Zhang, P. Croteau, T. Onasch, L. Williams, *et al.*, *Second ARM Aerosol Chemical Speciation Monitor Users' Meeting Report*, 2020.

25 D. C. Montgomery, *Design and Analysis of Experiments*, Limusa Wiley, 2004, vol. 46, DOI: 10.1080/00224065.2014.11917962.

26 C. Wu, R. A. Brown, Z. E. Brown, H. Trounce, E. J. Horchler, L. Wang, *et al.*, A new oxidation flow reactor for the measurements of secondary aerosol formation:

Characterisation and a case study, *Atmos. Environ.*, 2023, **309**, 119886, DOI: 10.1016/J.ATMOSENV.2023.119886.
27 D. Mitroo, Y. Sun, D. P. Combest, P. Kumar and B. J. Williams, Assessing the degree of plug flow in oxidation flow reactors (OFRs): A study on a potential aerosol mass (PAM) reactor, *Atmos. Meas. Tech.*, 2018, **11**, 1741–1756, DOI: 10.5194/AMT-11-1741-2018.
28 T. Pan, A. T. Lambe, W. Hu, Y. He, M. Hu, H. Zhou, *et al.*, A comprehensive evaluation of enhanced temperature influence on gas and aerosol chemistry in the lamp-enclosed oxidation flow reactor (OFR) system, *Atmos. Meas. Tech.*, 2024, **17**, 4915–4939, DOI: 10.5194/AMT-17-4915-2024.
29 Z. Peng, D. A. Day, A. M. Ortega, B. B. Palm, W. Hu, H. Stark, *et al.*, Non-OH chemistry in oxidation flow reactors for the study of atmospheric chemistry systematically examined by modeling, *Atmos. Chem. Phys.*, 2016, **16**, 4283–4305, DOI: 10.5194/ACP-16-4283-2016.
30 W. Liu, X. He, S. Pang and Y. Zhang, Effect of relative humidity on O3 and NO2 oxidation of SO2 on α-Al2O3 particles, *Atmos. Environ.*, 2017, **167**, 245–253, DOI: 10.1016/J.ATMOSENV.2017.08.028.
31 Y. Zhang, S. Tong, M. Ge, B. Jing, S. Hou, F. Tan, *et al.*, The influence of relative humidity on the heterogeneous oxidation of sulfur dioxide by ozone on calcium carbonate particles, *Sci. Total Environ.*, 2018, **633**, 1253–1262, DOI: 10.1016/J.SCITOTENV.2018.03.288.
32 J. Lelieveld, F. J. Dentener, W. Peters and M. C. Krol, Hydroxyl radicals maintain the self-cleansing capacity of the troposphere, *Atmos. Chem. Phys. Discuss.*, 2004, **4**, 3699–3720, DOI: 10.5194/acpd-4-3699-2004.
33 M. Li, E. Karu, C. Brenninkmeijer, H. Fischer, J. Lelieveld and J. Williams, Tropospheric OH and stratospheric OH and Cl concentrations determined from CH4, CH3Cl, and SF6 measurements, *npj Clim. Atmos. Sci.*, 2018, **1**, 29, DOI: 10.1038/s41612-018-0041-9.
34 T. Nah, R. C. Mcvay, X. Zhang, C. M. Boyd, J. H. Seinfeld and N. L. Ng, Influence of seed aerosol surface area and oxidation rate on vapor wall deposition and SOA mass yields: a case study with α-pinene ozonolysis, *Atmos. Chem. Phys.*, 2016, **16**, 9361–9379, DOI: 10.5194/acp-16-9361-2016.
35 J. H. Seinfeld and S. N. Pandis, *Atmospheric Chemistry and Physics: From Air Pollution to Climate Change*, Wiley, 2016.
36 Z. Peng, D. A. Day, H. Stark, R. Li, J. Lee-Taylor, B. B. Palm, *et al.*, HOx radical chemistry in oxidation flow reactors with low-pressure mercury lamps systematically examined by modeling, *Atmos. Meas. Tech.*, 2015, **8**, 4863–4890, DOI: 10.5194/amt-8-4863-2015.
37 T. Hohaus, U. Kuhn, S. Andres, M. Kaminski, F. Rohrer, R. Tillmann, *et al.*, A new plant chamber facility, PLUS, coupled to the atmosphere simulation chamber SAPHIR, *Atmos. Meas. Tech.*, 2016, **9**, 1247–1259, DOI: 10.5194/AMT-9-1247-2016.
38 H. Czech, O. Popovicheva, D. G. Chernov, A. Kozlov, E. Schneider, V. P. Shmargunov, *et al.*, Wildfire plume ageing in the Photochemical Large Aerosol Chamber (PHOTO-LAC), *Environ. Sci.:Processes Impacts*, 2024, **26**, 35–55, DOI: 10.1039/D3EM00280B.
39 J. Cao, Q. Wang, L. Li, Y. Zhang, J. Tian, L. W. A. Chen, S. S. H. Ho, X. Wang, J. C. Chow and J. G. Watson, Evaluation of the Oxidation Flow Reactor for particulate matter emission limit certification, *Atmos. Environ.*, 2020, **224**, 117086, DOI: 10.1016/J.ATMOSENV.2019.117086.
40 E. A. Bruns, M. Krapf, J. Orasche, Y. Huang, R. Zimmermann, L. Drinovec, *et al.*, Characterization of primary and secondary wood combustion products generated under different burner loads, *Atmos. Chem. Phys.*, 2015, **15**, 2825–2841, DOI: 10.5194/acp-15-2825-2015.
41 B. Bonn and G. K. Moortgat, Atmospheric Chemistry and Physics New particle formation during α-and β-pinene oxidation by O 3 , OH and NO 3 , and the influence of water vapour: particle size distribution studies, *Atmos. Chem. Phys.*, 2002, **2**, 183–196.
42 M. Simon, L. Dada, M. Heinritzi, W. Scholz, D. Stolzenburg, L. Fischer, *et al.*, Molecular understanding of new-particle formation from α-pinene between − 50 and +25 • C, *Atmos. Chem. Phys.*, 2020, **20**, 9183–9207, DOI: 10.5194/acp-20-9183-2020.